MATERIALS SCIENCE

An ultralight, pulverization-free integrated anode toward lithium-less lithium metal batteries

Chao-Hui Zhang[1,2], Yu-Jie Guo[1], Shuang-Jie Tan[1], Yu-Hao Wang[1,2], Jun-Chen Guo[1,2], Yi-Fan Tian[1,2], Xu-Sheng Zhang[1,2], Bo-Zheng Liu[3], Sen Xin[1,2], Juan Zhang[1,2]*, Li-Jun Wan[1,2]*, Yu-Guo Guo[1,2]*

The high-capacity advantage of lithium metal anode was compromised by common use of copper as the collector. Furthermore, lithium pulverization associated with "dead" Li accumulation and electrode cracking deteriorates the long-term cyclability of lithium metal batteries, especially under realistic test conditions. Here, we report an ultralight, integrated anode of polyimide-Ag/Li with dual anti-pulverization functionality. The silver layer was initially chemically bonded to the polyimide surface and then spontaneously diffused in Li solid solution and self-evolved into a fully lithiophilic Li-Ag phase, mitigating dendrites growth or dead Li. Further, the strong van der Waals interaction between the bottommost Li-Ag and polyimide affords electrode structural integrity and electrical continuity, thus circumventing electrode pulverization. Compared to the cutting-edge anode-free cells, the batteries pairing $LiNi_{0.8}Mn_{0.1}Co_{0.1}O_2$ with polyimide-Ag/Li afford a nearly 10% increase in specific energy, with safer characteristics and better cycling stability under realistic conditions of 1× excess Li and high areal-loading cathode (4 milliampere hour per square centimeter).

INTRODUCTION

Spurred by the emerging electric vehicle market, rechargeable lithium batteries technology experiences progressive breakthroughs (*1*–*10*). To date, the most cutting-edge batteries (anode-free batteries coupled with Li-rich cathode) could output an estimated cell-level energy density of more than 500 Wh kg^{-1} (*11*–*13*). Nonetheless, there seems to be an endless desire for "longer mileage" or emerging electric aircraft transportation, the improvements in higher energy density are constantly being demanded.

In a practical battery, the positive/negative electrodes (including the collector) account for approximately 70 wt % of the total mass of the battery. Increasing the amount of extractable lithium per mass unit in the active material or minimizing the proportion of inactive material (e.g., collector) at the electrode level can enhance the energy density of the battery (*14*–*20*). On the cathode side, the theoretical capacity of layered Li-rich materials is approaching their upper limit due to the limitations of topochemical Li^+ intercalation chemistry (*21*–*24*). Thus, it is now challenging to boost specific energy by a further 10% through improvements at the cathode. On the anode side, by adopting the emerging anode materials with different lithium storage mechanisms (e.g., silicon and metal lithium), the specific capacity of anode (calculated on the active material) has been markedly increased (*25*–*28*). Nevertheless, when evaluating the overall specific capacity of the electrode by considering both the active and inactive materials (current collectors) in the anode, the high capacity advantage of metal-Li is discounted due to the widespread utilization of heavy copper collectors. For example, in batteries using 20-μm Li metal on Cu collector (Cu-20Li) as the anode, the total anode constitutes less than 20 wt % of the battery (fig. S2), while the mass of inactive material in the anode exceeds 75 wt %. Even in an anode-free battery (Cu-0Li), despite the mass ratio of the anode in the battery has been minimized to 16 wt %, this 16 wt % comprises exclusively inactive components (*11*, *12*, *29*). Therefore, by the construction of a lightweight integrated anode with an increased total-anode capacity, it may be possible to boost the specific energy of Li metal batteries to a higher level (Fig. 1A).

In the context of conserving lithium resources and meeting the demand for higher battery-specific densities, it is imperative to minimize the amount of lithium metal used in lithium metal batteries (LMBs) for practical applications. Nevertheless, such anode-less batteries operating under lithium-limited conditions, have encountered challenges, particularly with a serious pulverization problem that jeopardizes their long-term cyclability. Pulverization in LMBs mainly manifested in two aspects (Fig. 1B). The first one is associated with the growth of lithium dendrites. Upon inhomogeneous Li stripping from the underneath, the Li dendrites break off and detach from the collector, forming "dead" Li (*30*, *31*). The massive pulverized Li pieces accumulated at the upper layer of the electrode, causing the dead Li pulverization, which results in rapid capacity decay and deteriorated cycling efficiency. The introduction of highly lithophilic alloy (e.g., Ag, Al, Mg, and In) was proven effective to regulate Li nucleation and minimize the formation of dendrite or dead Li (*32*–*36*). However, the huge volume change of the alloy (or pure lithium) during the repeated Li plating/stripping may lead to the separation of the entire active material from the collector or, even worse, the disintegration of the electrode (*37*, *38*). This is the so-called electrode electro-chemo-mechanical pulverization (referred to as electrode pulverization), which can directly lead to a "cliff jump" in capacity and quick battery failure. In particular, the electrode pulverization behavior becomes even more evident under the limited conditions of low negative/positive capacity ratio (N/P ratios) required for a high specific energy of battery. Therefore, the ideal lithium metal integrated anode should not only be lightweight but be functional to circumvent the pulverization problems so as to gain an extended cycle life.

In this work, a lightweight polyimide-nanosilver/Li (referred to as PI-Ag/Li) was developed as a functionalized, integrated anode for

[1]CAS Key Laboratory of Molecular Nanostructure and Nanotechnology, CAS Research/Education Center for Excellence in Molecular Sciences, Beijing National Laboratory for Molecular Sciences (BNLMS), Institute of Chemistry, Chinese Academy of Sciences (CAS), Beijing 100190, P. R. China. [2]School of Chemical Sciences, University of Chinese Academy of Sciences, Beijing 100049, P. R. China. [3]Tianjin Lishen Battery Joint-Stock Co. Ltd., Tianjin 300384, P. R. China.
*Corresponding author. Email: zhangjuan120@iccas.ac.cn (J.Z.); wanlijun@iccas.ac.cn (L.-J.W.); ygguo@iccas.ac.cn (Y.-G.G.)

metal Li batteries. Inspiringly, using PI-Ag/Li as an integrated anode, the cell-level specific energy of a full cell was calculated to increase by a further ~10% compared to the anode-free cell using a copper anode (delivering an estimated energy density of ~620 Wh kg^{-1}). PI-Ag/Li integrated anode was obtained by chemically anchoring silver monolayers to PI matrix through a scalable ion-ligand exchange process, followed by lamination with an ultrathin lithium foil or electrodeposition. In-depth study on the Li stripping/plating process reveals that the underlying Ag atoms spontaneously diffused upward at the early electrochemical stage. This self-evolving process renders PI-Ag/Li fully lithiophilic to enable uniform lithium deposition and mitigates dead Li pulverization, as illustrated in Fig. 1C. Furthermore, owing to the strong van der Waals force between silver atom and imide group from PI matrix (Li-Ag···O═C), the electrode pulverization was simultaneously mitigated. Benefiting from the dual anti-pulverization function, the PI-Ag/Li||$LiNi_{0.8}Mn_{0.1}Co_{0.1}O_2$ (NCM811) full cell shows an excellent cycling performance with 80% capacity retention over 500 cycles (with N/P ratio of 5). Even under a highly practical condition of high-areal loading cathode (20 mg cm^{-2}) and ultralow N/P ratio (1.0), PI-Ag/Li||NCM811 cells still maintain a remarkably stable cycling with capacity retention of 90% over 170 cycles. We also assembled pouch cells with a PI-Ag/Li anode and an NCM811, which shows good cycling performance under realistic testing conditions. In addition, the unique thermal insulation of PI can effectively block the vertical spread of heat during thermal abuse of a pouch cell, rendering the high-energy LMBs flame retardant functionality.

RESULTS

Characterization of the PI-Ag

The mass density of polyimide (1.42 g cm^{-3}) is much lower than that of copper metal (8.9 g cm^{-3}), which indicates the ultralightweight nature of our integrated anode. PI-Ag matrix was synthesized through a three-step chemical reaction (note S1). The detailed synthesis process was illustrated schematically in Fig. 2A. The first step (step I, Fig. 2, B and C) was the alkali catalysis hydrolysis of PI in KOH solution to form potassium carboxylate and amide. The second step (step II, Fig. 2, C and D) involves adsorption of Ag^+ and ion-ligand exchange reaction in silver ammonia solution, with formation of PI-Ag^+. The third step (step III, Fig. 2, D and E) was the redox reaction from Ag ions to metallic Ag nanoparticles (NPs) with L-ascorbic acid as the reducing agent. The chemical reaction process was monitored by x-ray photoelectron spectroscopy (XPS) techniques. For the pristine PI film, only three elements (C, O, and N) were detected from XPS spectra in Fig. 2F and fig. S3. After the immersion in KOH, the C *1s* spectrum shows that the imide carbonyl peak located at 288.7 eV disappears, and the signal peaks of amide carbonyl at 287.7 eV and carboxylate at 290.2 eV are observed, respectively. At the same time, the presence of the K^+ peaks indicates the ring-opening and hydrolysis of imine (Fig. 2G and fig. S4). Subsequently, the peak of K^+ disappears from the XPS spectra and is replaced by the Ag^+, validating the ion-ligand exchange process (Fig. 2H). After the redox reaction, the silver peak in Ag *3d* spectrum shifts to a lowered energy, suggesting the reduction of Ag ions to metallic Ag (Fig. 2I and fig. S5). Ex situ atomic force microscopy (AFM) technique was used to visualize the chemical reaction process. Figure 2 (J to M) shows that the surface of PI, PI-K^+, and PI-Ag^+ are homogeneous, indicating the complete surface reaction and Ag NP nucleation. Scanning electron microscopy (SEM) images (figs. S6 and S7) show that Ag NPs (mainly in agglomerates state) are uniformly and continuously dispersed on the PI film. The Ag layer is approximately 1 μm in thickness. The weight ratio of Ag on PI is ~24 wt % resultant from the Thermogravimetry analysis in fig. S8. The electron conductivity of PI-Ag matrix is measured to be 4.6×10^7

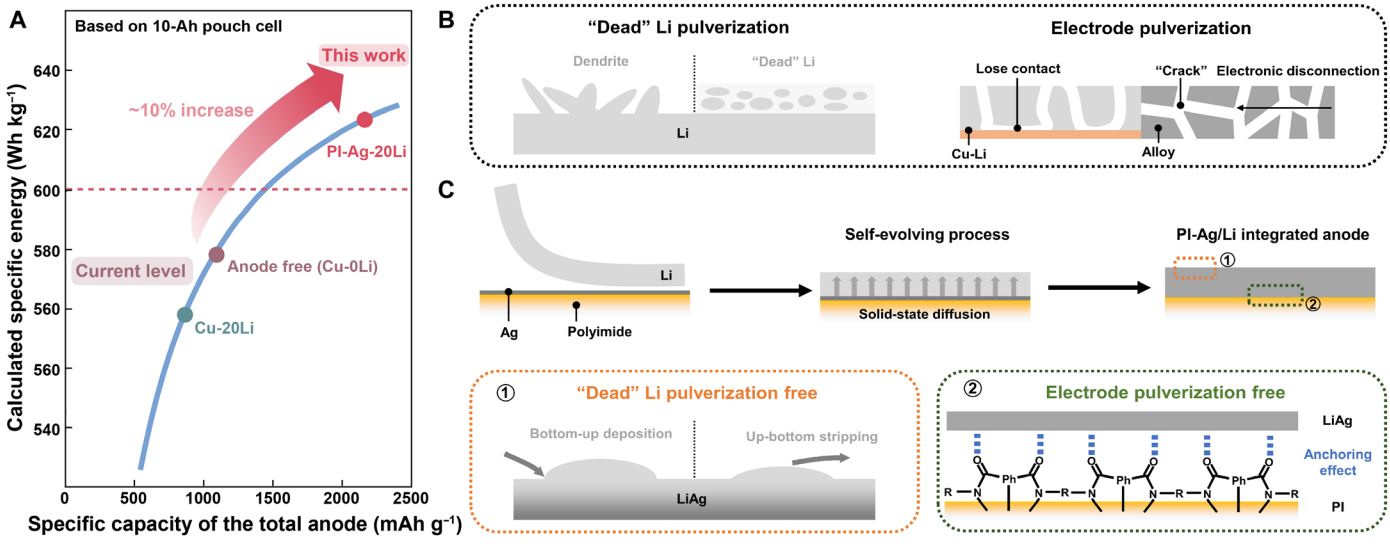

Fig. 1. High specific energy advantages of LMBs using PI-Ag/Li integrated anodes and the schematic of the dual anti-pulverization mechanism of the integrated anodes. (**A**) Comparison of the specific energy of a 10-Ah pouch cell with lithium-rich cathodes coupled to different lithium metal anodes and the specific capacity of the total anode in the battery. LMBs using Li-rich cathode and PI-Ag-20Li anode afford a nearly 10% improvement in specific energy compared to the state-of-the-art anode-free batteries using Cu-0Li anode. The mass of the total anode comprises both active and inactive materials, and the value of the areal capacity for calculation is set to 4 mAh cm^{-2} (refer to table S1 and fig. S1 for more calculation details). (**B**) Schematic of the anode pulverization problems for most lithium-limited LMBs. (**C**) Schematic of how self-evolved PI-Ag/Li integration functions to inhibit dead Li or electrode pulverization.

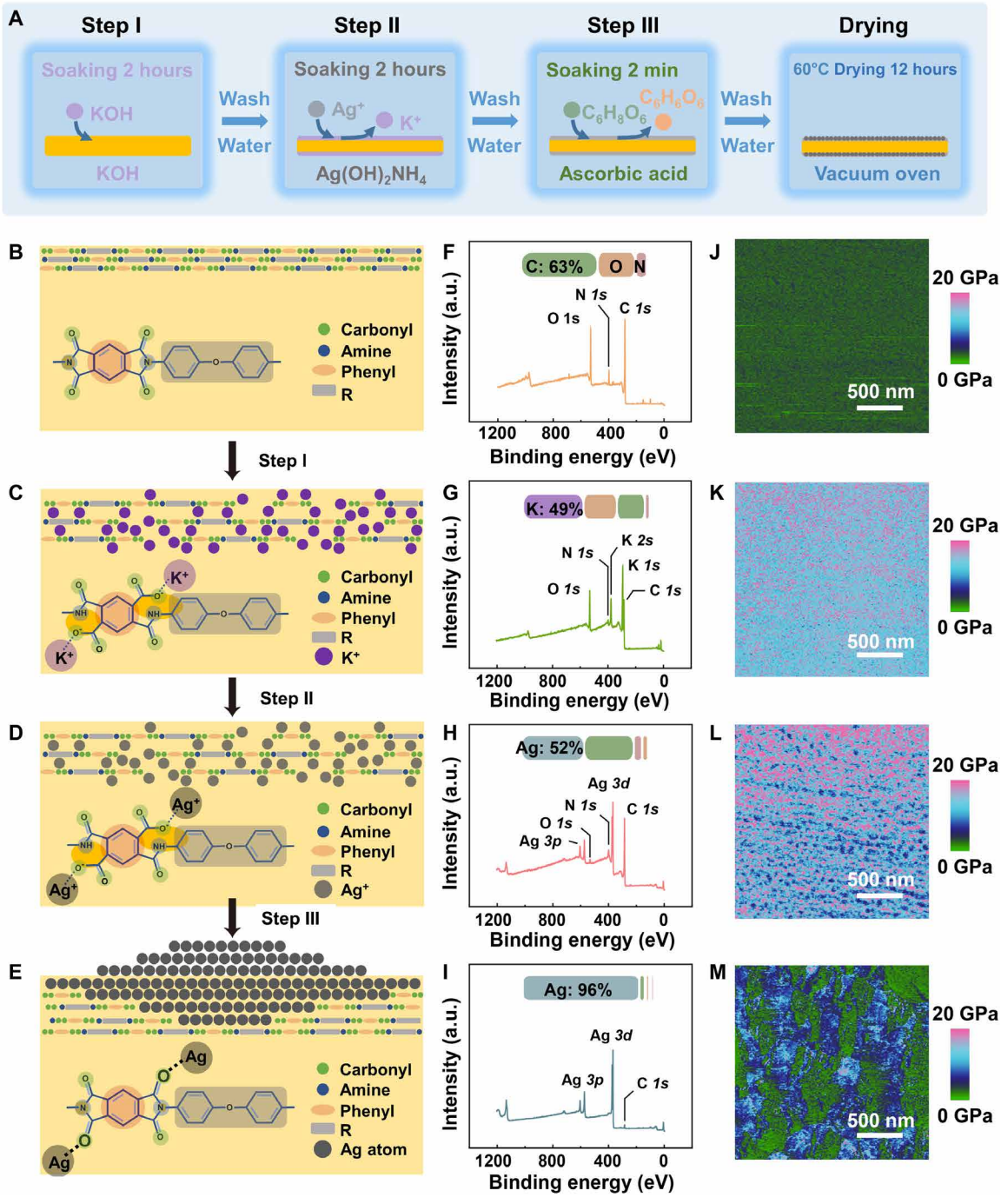

Fig. 2. Characterizations of the PI-Ag functional substrate during preparation. (**A**) Schematic of the fabrication of Ag-PI. Schematics of the composition evolution of (**B**) pristine PI, (**C**) PI-K^+, (**D**) PI-Ag^+, and (**E**) PI-Ag during preparation and the corresponding chemical structures. XPS spectra and component analysis of (**F**) PI, (**G**) PI-K^+, (**H**) PI-Ag^+, and (**I**) PI-Ag (the bar graphs show the proportion of each element). AFM images of the (**J**) PI, (**K**) PI-K^+, (**L**) PI-Ag^+, and (**M**) PI-Ag. a.u., arbitrary units.

S m^{-1} by four-probe tester, which is comparable to Al foil or Cu foil (fig. S9), verifying its promising electronic conducting function.

In situ electrochemical lithiation behavior of PI-Ag

We first investigated the lithium plating/stripping behavior of PI-Ag functional substrate (Fig. 3A) by in situ electrochemical lithiation. Fig. 3 (B and C) shows the in situ x-ray diffraction (XRD) profiles (performed on a specialized Swagelok battery as shown in fig. S10) of PI-Ag-Li during the first cycle. Electrochemical testing was performed at a current density of 0.5 mA cm^{-2}, with lithiation first at a cutoff capacity of 5 mAh cm^{-2} and then delithiation at a cutoff voltage of 0.2 V. It reveals that the PI-Ag experienced a stepwise alloying and nucleation precipitation upon the lithiation process. At the early stage of lithiation, the diffraction peaks of $Li_{7.5}Ag$

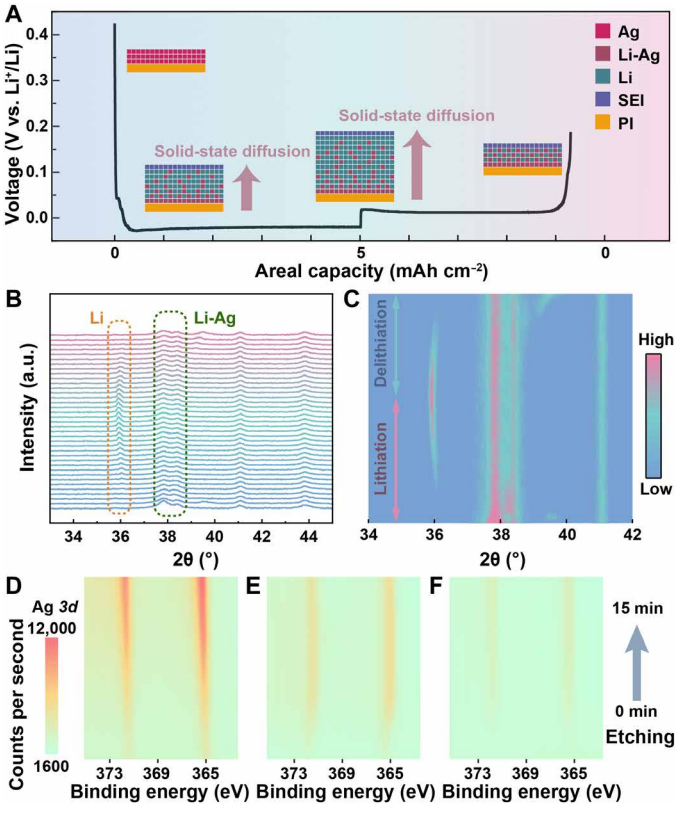

Fig. 3. Characterization of the PI-Ag-Li integrated anode by electrodeposition. (**A**) Galvanostatic charge/discharge voltage curves of PI-Ag during the initial lithiation-delithiation at 0.5 mA cm^{-2} with an areal capacity of 5 mAh cm^{-2}. Inset: The schematic for the solid diffusion of Ag atoms in Li solid solution during the lithiation-delithiation process. (**B**) In situ XRD patterns and (**C**) the waterfall plots of PI-Ag during the initial Li plating-stripping at 0.5 mA cm^{-2}. In-depth XPS spectra of the PI-Ag after a Li-deposition of (**D**) 2 mAh cm^{-2}, (**E**) 5 mAh cm^{-2}, and (**F**) 10 mAh cm^{-2}.

at 39.5° and $Li_{11.8}Ag$ at 39.2° appear for a while and then quickly vanish, demonstrating the initial Li-Ag alloying reaction (*39*). Upon further lithiation, the ultimate alloyed product of $Li_{20}Ag$ (38.6°) is identified and remains unchanged. Simultaneously, the diffraction peak of lithium metal at 36° appears and gradually intensifies, indicating the Li nucleation process initials. The delithiation process shows the opposite phase transition process, with $Li_{7.5}Ag$ as the final charging product. The spatial composition and distribution of alloy phase in the PI-Ag-Li upon electrodeposition were determined by in-depth XPS analysis. Figure 3 (D to F) presents the XPS depth profiling of the PI-Ag electrodes after plating with 2, 5, and 10 mAh cm^{-2}, respectively. The signal of Ag gradually intensifies as the sputtering depth approaches the interior (the underlying part of PI-Ag-Li). Energy-dispersive x-ray spectroscopy mapping shown in fig. S11 presents that the elemental Ag is uniformly distributed throughout the lithium layer. This implies that Ag atoms may spontaneously diffuse across the whole electrode during the initial electrochemical (de)lithiation process, driven by solid solution equilibrium. According to the lithium-silver phase diagram, silver has a large solubility in lithium which accounts for the spontaneous diffusion property of PI-Ag-Li. This self-evolution process leads to a fully lithiophilic integrated anode of PI-Ag-Li, and the uniformly distributed Li-Ag sites will spatially regulate the lithium deposition and inhibit dendrite growth.

To evaluate the dendrite-inhibiting functionality of PI-Ag-Li, the Li electrodeposition behavior was deeply investigated. As shown in fig. S12, the PI-Ag-Li exhibits a much lower lithium nucleation overpotential than that of copper foil (0.05 V versus 0.15 V) at a current density of 0.5 mA cm^{-2}. From SEM investigation, at a lithium deposition of 0.5 mAh cm^{-2}, the lithium nuclei on the copper foil present a rod-like structure, while the surface of the PI-Ag-Li presents a smooth and dendrite-free morphology (fig. S13, A and B). After electrodeposition with 4 mAh cm^{-2} of lithium, these rod-shaped lithium nuclei on copper developed into lithium dendrites, resulting in a loose and irregular deposition pattern. In comparison for PI-Ag, even at a high current density of 4 mA cm^{-2}, the deposition morphology remains flat and dense (fig. S13, C to F). For a better implementation of PI-Ag/Li, an ultrathin lithium foil (20 μm, 4 mAh cm^{-2}) was rolled on the PI-Ag matrix to obtain PI-Ag-20Li integrated anode. Energy dispersive spectroscopy (EDS) analysis was performed on the cross-sectional image of PI-Ag-20Li. The result shows that after 24 hours of placement, the silver atoms were uniformly distributed throughout the 20-μm-thick integrated electrode (fig. S14). This result was in accordance with the in-depth XPS spectra in fig. S15, demonstrating that Ag elemental can be detected at the uppermost of the composite anode (note that thin layers of lithium oxide are caused by short-term exposure to air). Therefore, it can be inferred that whether lithium is electrodeposited or rolled on PI-Ag (lithium amount should be within 10 mAh cm^{-2}), the Ag atoms attached to PI will spontaneously diffuse upward until reaching a thermodynamic equilibrium, forming a homogeneous, fully lithiophilic PI-Ag-Li integration, which functions to guide a uniform Li deposition. Furthermore, the strong interaction between Ag atom and PI can firmly hold the bottommost layer of silver atoms in place (discussed below), thereby guaranteeing a sufficient electron transfer capability of the integrated anode.

Performance of half-/full cells using PI-Ag/Li under realistic conditions

We first investigated the Li plating/stripping property in half-cells using Li||PI-Ag and Li||Cu. When applied in a button cell, a small piece of the PI-Ag film was folded to achieve electrical contact with the steel shell (Fig. 4A and fig. S16). Coulombic efficiency is an important index that determines the cycle life of a lithium metal anode in practical batteries, in which the lithium source is limited. The test protocol for average Coulombic efficiency was adopted from a previous report by Zhang's group (*40*). The calculated average Coulombic efficiency of Li||Cu and Li||PI-Ag are 83.3% and 94.6%, respectively (Fig. 4B). The increase in average Coulombic efficiency accounts for the improved Li deposition behavior of the PI-Ag-Li and would promote to an extended cycling life in a "limited lithium source" full battery system. Electrochemical impedance spectroscopy tests were further carried out on PI-Ag/Li||Li half-cells before cycling, with Cu/Li||Li as a comparison. Referring to fig. S17, the half-cell using PI-Ag/Li anode shows a smaller overall impedance compared to the half-cell with Cu/Li anode, indicating better kinetics with our integrated anode. We then investigated the performance of PI-Ag-Li integrated anode in a full cell with NMC811 as a cathode. PI-Ag and Cu were first prelithiated with 8 mAh cm^{-2} of lithium, and the N/P ratio of the full cell is 5. As demonstrated in Fig. 4C and fig. S18, the capacity of Cu-Li||NCM811 full cell was stable at the initial cycles (1 to 50 cycles) but

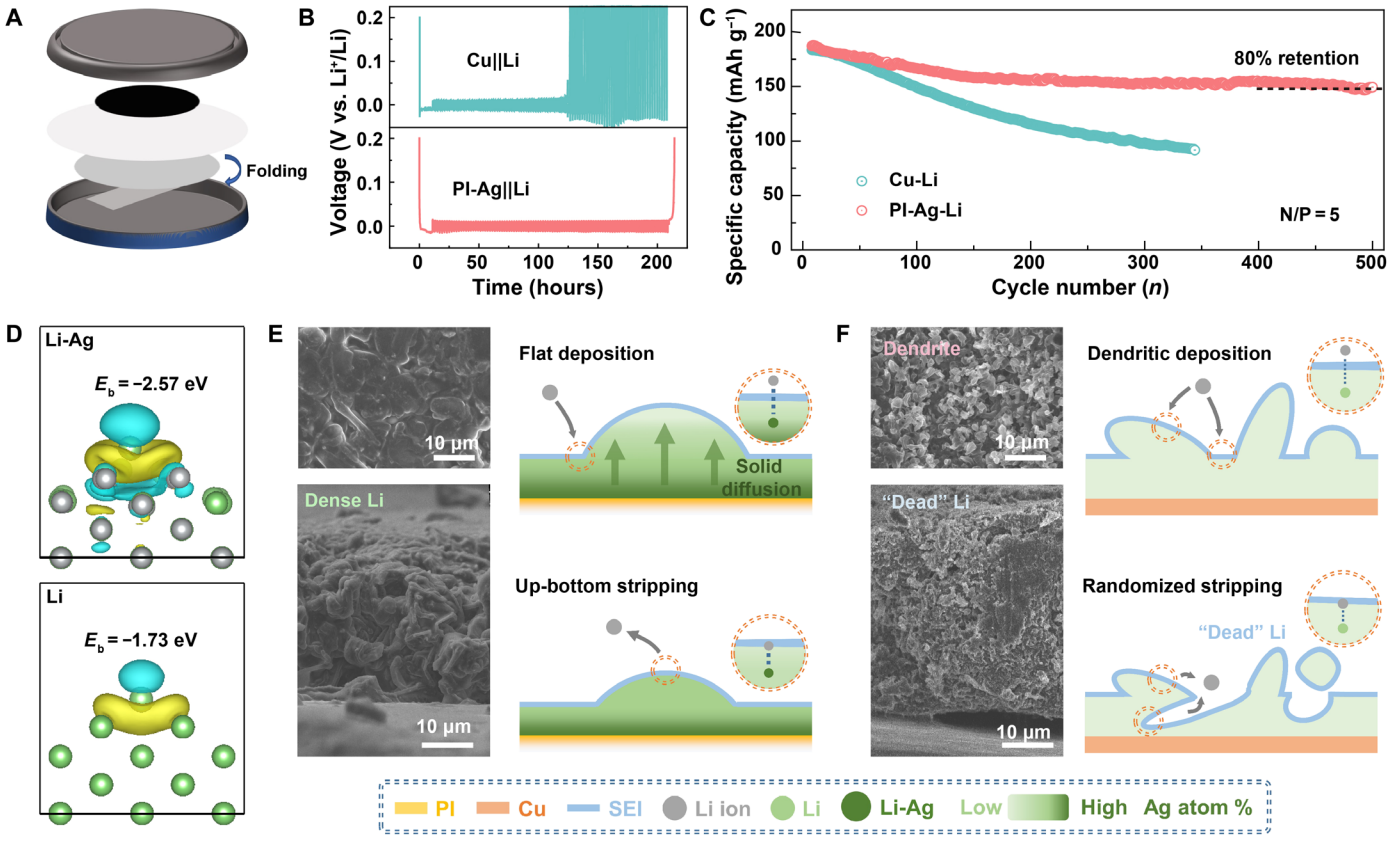

Fig. 4. Electrochemical performance of half-cells and full cells with PI-Ag-Li integrated anode and the stabilization mechanism of Li deposition. (**A**) Schematics of cell assembly in a coin cell. (**B**) Average Coulombic efficiency test protocol in Li||Cu and Li||PI-Ag half-cells to calculate the average Coulombic efficiency. (**C**) Long-term cycling performance of the batteries using NCM811 (1.5 mAh cm^{-2}) paired with a Li-deposited Cu anode (8 mAh cm^{-2}) and PI-Ag-Li anode (8 mAh cm^{-2}). Constant current constant voltage (CCCV) cycling is performed at 0.5C (1 C = 200 mA g^{-1}), with the voltage window of 2.8 to 4.3 V versus Li^+/Li. (**D**) The deformation charge density and the atom structures of Li adsorption on the Li-Ag (100) and Li (100). Inset: The corresponding binding energies. The top-view and cross-sectional SEM images of (**E**) PI-Ag-Li and (**F**) Cu-Li anode after 50 cycles in full cells and schematics of the stabilization mechanism for Li deposition/stripping.

then decayed abruptly, and the cell quickly failed after 100 cycles. This could be mainly due to the irregular Li plating/stripping which gives rise to a rapid consumption of active lithium in the cell. When the inventory Li is exhausted, the cell immediately fails. In sharp contrast, cells with the PI-Ag-Li integrated anode show an excellent cycling performance and high Coulombic efficiency, delivering stable capacity for over 500 cycles (with over 80% capacity retention). The superior long-term cycling stability demonstrates the function of PI-Ag-Li to improve the utilization of active lithium.

To better understand the important role of PI-Ag-Li on stabilizing the Li deposition, interface analysis was first conducted on the cycled PI-Ag-Li and Cu-Li anodes in full cells. From the XPS depth results in fig. S19, the two anodes show similar SEI structures, with organic components dominating the exterior of SEI (fig. S19, A and B, and table S2) and inorganics (e.g., LiF) dominating the interior of SEI. Notably, the Ag *3d* spectra are consistently detected in PI-Ag-Li, and the signal becomes even stronger with increasing the etching depth (fig. S19, C and D). After 10 min of etching, the characteristic peak of Li-Ag alloy (365.5 and 371.3 eV) appears, confirming the self-evolution nature of the integrated anode during electrochemical process as evidenced by the half-cell analysis. First-principles calculations theoretically explain how the fully lithiophilic PI-Ag-Li functions to regulate lithium plating/stripping. Figure 4D displays the deformation charge densities and the corresponding binding energies of Li on the Li (110) surface and Li-Ag alloy (110) surface, which are −1.73 and −2.57 eV, respectively. The stronger adsorption energy between Li-Ag and Li indicates that Li prefers to nucleate surrounding Ag atoms, and thus, the upward diffusion of Ag atoms was favorable for directing the homogeneous lithium nucleation and growth. In Fig. 4E, during the Li stripping process, the stronger binding energy induces lithium to be preferentially stripped from the surrounding of the silver atoms in an "up-bottom" pattern. Such "riveting effect" of Li-Ag phase prevents the formation of dead Li and thus contributes to a denser and flatter deposition morphology as evidenced by the cross-sectional SEM image. As for Cu-Li anode without riveting effect shown in Fig. 4F, the newly exposed lithium at the root of Cu-Li may preferentially detach from the current collector as the electrolyte gradually infiltrates, which will cause the lithium above the stripped Li to lose activity and form dead Li. The gaps generated by dead Li stacking make Cu-Li thicker than PI-Ag-Li after 50 cycles. Therefore, it can be inferred that the exceptional cycling stability was uniquely ascribed to the self-evolution of Li-Ag alloy in the PI-Ag-Li anode which favors a well-regulated Li deposition and thus circumvents the dead Li pulverization problem.

To better evaluate the potential application of PI-Ag-Li in practical LMBs, 20-μm Li was rolled on PI-Ag by a scalable roll-to-roll manufacturing to obtain PI-Ag-20Li anode. Stripping/plating measurements were carried out in half-cells (Li||Cu-20Li and Li||PI-Ag-20Li) to validate the functionality of the PI-Ag-Li anode. A practical capacity of lithium at a high current density (2 mAh cm^{-2} at a current density of 2 mA cm^{-2}) was repeatedly deposited/stripped in each discharge/charge cycle. The upper limit of the charging voltage is set at 0.4 V. Typically, because of the limited amount of lithium in the system (4 mAh cm^{-2}), a surge of the charging voltage to 0.4 V indicates the complete consumption of available lithium from the counter electrode during the cycle. Figure 5A shows the voltage profiles as a function of time. The half-cell using Cu-Li exhibits huge overpotential fluctuations, and the voltage quickly reaches 0.4 V at 400 hours. This could be attributed to the lithiophobic of Cu matrix that leads to an irregular Li plating/stripping and quick lithium exhaustion. In contrast, the PI-Ag-20Li shows very stable voltage profiles for over 1000 hours with a much lower overpotential compared to Cu-Li. The improvement in cycling life verifies the effectiveness of the self-evolved PI-Ag-20Li in regulating homogeneous Li deposition without dendrite formation. This is consistent with the results collected from average Coulombic efficiency analysis. More practical and harsh condition was tested to verify the practicality implementation of the PI-Ag-20Li integrated anode. The mass loading of the NCM811 cathode material was 20 mg cm^{-2} (areal capacity: 4 mAh cm^{-2}) and was used to match PI-Ag-20Li, Cu-20Li, and 20Li-Ag alloy anodes to assemble lithium metal full cells. The N/P ratio of the full cell is 1.0. The cycle performance of the full cells was performed at 0.5 C rate (1.0 C = 200 mA g^{-1}). To meet the demanding cycling requirements under realistic conditions, it is essential to minimize the influence of other factors, including side reactions between lithium and the electrolyte. For this reason, we chose a localized high concentration electrolyte (LHCE) with low reactivity to lithium, which

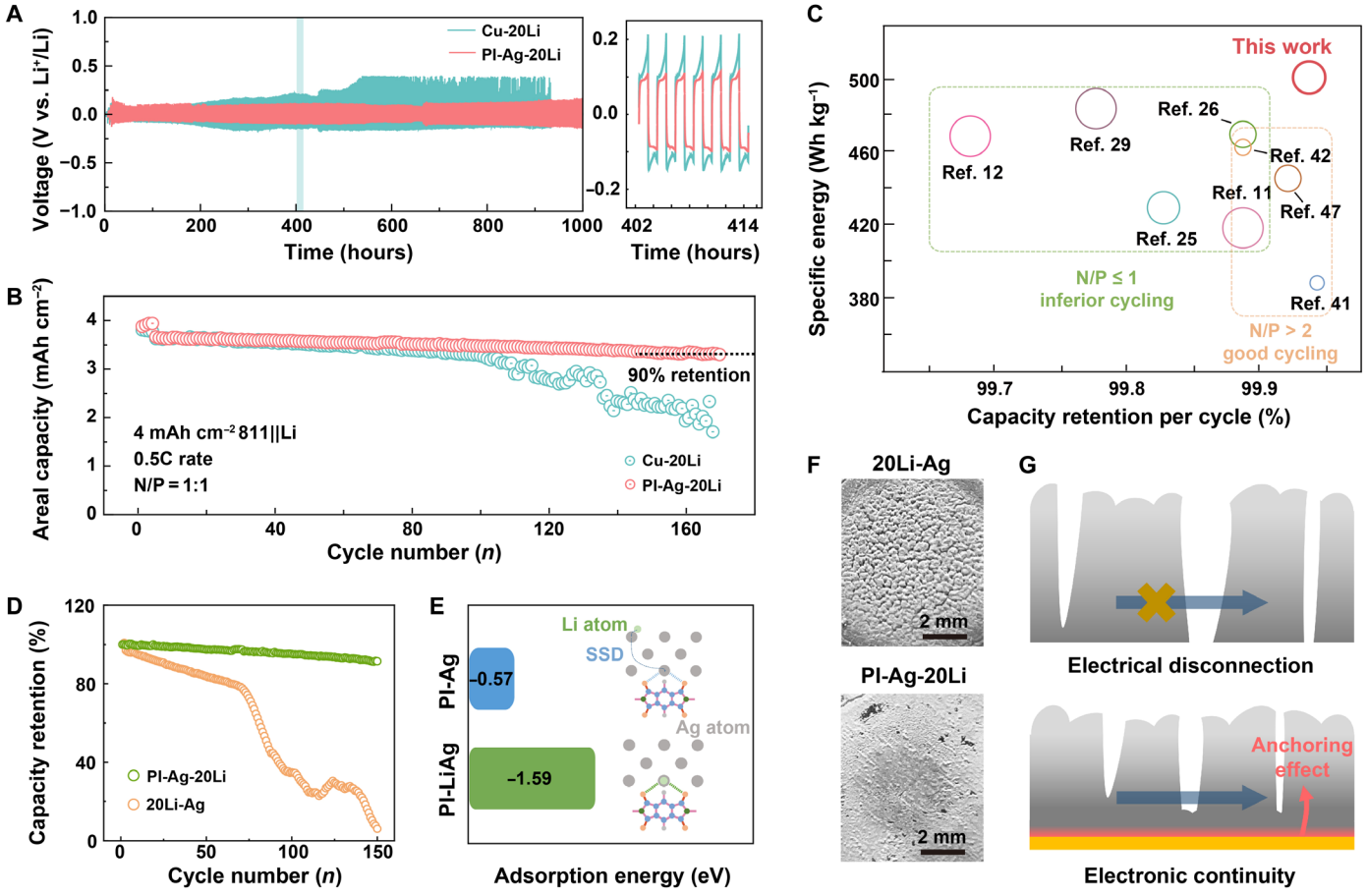

Fig. 5. Performance of PI-Ag-20Li symmetric cells and NCM811||PI-Ag-20Li full cells under a realistic test condition. (**A**) The Li deposition/stripping voltage curves of Cu-20Li and PI-Ag-20Li symmetrical cells at 2 mA cm^{-2} with an areal capacity of 2 mAh cm^{-2}. The insets show the high-resolution voltage profiles at specific times. (**B**) Cycling performance of full cells with 4 mAh cm^{-2} NCM811 as the cathode and PI-Ag-20Li or Cu-20Li as the anode. The test protocol is CCCV at 0.5 C rate (1 C = 200 mA g^{-1}) with the voltage window of 2.8 to 4.3 V. (**C**) Comparison of full-cell specific density versus per-cycle capacity retention between PI-Ag-Li||NCM 811 full cell in this work and recently reported lithium-less full cells (projected by a 10-Ah pouch cell). Note that the area of the circumference represents the N/P ratio in the full cell, and only the reported data with N/P ratios less than 5 are involved in the graph. Note that the specific density is extrapolated from a 10-Ah pouch cell, see table S4 (*11*, *12*, *25*, *26*, *29*, *41*, *42*, *47*) for the detailed parameters. (**D**) Capacity retention of full cells with 4 mAh cm^{-2} NCM811 paired with PI-Ag-20Li and 20Li-Ag alloy anode. (**E**) Adsorption energy between polyimide and Ag or Li-Ag alloy and solid-solution diffusion process of Li during lithium deposition. Polyimide polymerization degree is $n = 1$, Ag crystal surface is (111), and Li-Ag alloy crystal surface is (110). (**F**) The optical images of the entire electrode of PI-Ag-20Li and 20Li-Ag after 10 cycles in full cells. (**G**) The schematics showing how PI-Ag/Li integrated anode mitigate electrode pulverization in a lithium-limited system as compared to alloy anodes.

is commonly used in lithium-less systems. As shown in Fig. 5B and fig. S20, the cell with Cu-Li begins to decay after 100 cycles, with much lower Coulombic efficiency. In contrast, PI-Ag-20Li||NCM811 full cell delivers a high average capacity retention of 99.94% per cycle and a stable cycling performance over 170 cycles (with 90% capacity retention). The rate capability of PI-Ag-Li||NMC811 and Cu-Li||NCM811 is evaluated in fig. S21, PI-Ag-Li||NCM811 maintained a high discharge capacity of 124 mAh g^{-1} at 5 C rate, whereas the capacity of the Cu-Li||NCM811 was only 75 mAh g^{-1}. To highlight the superiority of our results compared with recently published work, we summarize and compare the full-cell performance at both the cell level and anode level. Figure S22 and table S3 give the comparison of our integrated anode with recently reported lithium metal anodes (*11*, *19*, *25*, *26*, *35*, *41*–*46*), in terms of total-anode specific capacity (calculated by dividing the areal capacity by the total anode mass) and cycling performance in a full cell. Our integrated anode demonstrates superior comprehensive performance in total anode specific capacity and full-cell cycling. We then compare the performance of a projected high-energy Li metal cell with lithium-less anodes and NCM811 cathodes under realistic conditions of high areal capacity, low N/P ratio, and lean electrolyte supply (*11*, *12*, *25*, *26*, *29*, *41*, *42*, *47*). The graph in Fig. 5C illustrates cell-level energy density, derived from a 10-Ah pouch cell, plotted against capacity retention per cycle. The majority of the data within the orange line indicates a preference for a high N/P ratio (ranging from 3 to 5) or a low cathode areal capacity (<3 mAh cm^{-2}) to mitigate concerns such as uncontrolled growth of dead lithium or electrode pulverization, leading to improved capacity retention. Nevertheless, this approach may compromise the specific energy of the battery. In the green circle region, lithium-limited systems sacrifice average capacity retention (below 99.8%) for higher specific energy. In comparison, our cells, highlighted in Fig. 5C, achieve high specific energy and excellent cycling stability (99.94% capacity retention per cycle) simultaneously.

Morphology evolution after cycling was studied for Cu-20Li, 20Li-Ag alloy anode, and PI-Ag-20Li integrated anodes in the full cells. As revealed from top-view SEM images in fig. S23, the Cu-20Li anode displays a loose structure covered with massive mossy Li dendrite, which accounts for the low Coulombic efficiency and rapid capacity decay. In the case of 20Li-Ag alloy anode in Fig. 5D, the full cell assembled with 20Li-Ag alloy anode can only operate for 60 cycles before a "cliff-jumping" capacity decay occurs, which suggested that the PI matrix played a key role in improving the battery cyclability. To explore how the PI-Ag/Li functions on an anti-pulverization property in such low N/P condition, the binding energies of PI with Li-Ag alloy and Ag were calculated by density functional theory (DFT) methods. The results reveal that the Li-Ag alloy (110) has a stronger adhesion force to PI than Ag (111) through the van der Wale forces between the oxygen from carbonyl (O═C) and the Ag and Li (Fig. 5E; binding energy: 1.59 eV versus 0.57 eV). Therefore, it can be inferred that during the self-evolution process, lithium diffuses into the interface between PI film and the silver to form Li-Ag alloy, resulting in a strengthened interaction force between the alloy and the PI film (shown in fig. S24). The entire electrode presents an overall fragmentation state as confirmed by optical images (Fig. 5F). The result implies that although lithiophilic Ag alloy was proven effective in mitigating the dendrite formation, the huge volumetric change during repeated plating/stripping may cause disastrous mechanical pulverization of the electrode, thereby resulting in electrical disconnection and rapid cell failure. In comparison, the PI matrix can firmly anchor the Li-Ag alloy layer upon the repeated Li plating/stripping, thereby effectively preventing the upper layer of active material from fragmentation of the integrated anode, thus suppressing the electrode pulverization. A practical pouch cell coupling NCM811 cathode exhibits stable cycling with capacity retention of over 90% after 45 cycles at 0.2 C and verifies the practical implementation of PI-Ag-20Li anode (figs. S25 and S26). The above analysis reveals that under the lithium-limited systems required for high energy density batteries, the mechanical pulverization of the electrode upon the electrochemical process is also a key factor deteriorating the performance of the full battery, in addition to the problem of "dead Li pulverization originated from dendrites growth." Our functional integrated anode conforming to the solid solution self-evolution mechanism can regulate lithium growth, eliminate the dead Li, and solve the dendrite pulverization. Simultaneously, the strong interaction between PI substrate and Li-Ag can circumvent the mechanical pulverization problem of the alloy anode, thus enabling the full battery stably cycle under a harsh N/P ratio of 1.0.

Battery safety in practical cells

The safety problem of next-generation high-energy LMBs has raised widespread concerns, especially regarding thermal runaway caused by overheating. Our PI-Ag-Li integrated anode enables the batteries with improved specific energy and extended cycle life while also rendering the advantages of superior safety. As shown in Fig. 6A, for a practical pouch cell consisting of multiple layers of PI-Ag-Li electrodes, in the occurrence of a localized thermal runaway, owing to the thermal insulation property of the PI substrate, heat will tend to propagate and dissipate along the surface of the layer rather than through the interlayer to the adjacent electrodes. In addition, self-extinguishing property of polyimide could further prevent the thermal abuse. To verify the above anticipation, the heat transfer process of PI-Ag substrate and conventional Cu substrate were simulated using COMSOL Multiphysics. For PI-Ag substrate, when exposed to a constant heat source, due to the good thermal conductivity of the surface silver layer, the heat is mainly transferred across the silver layer and hardly transferred longitudinally through the polyimide; thus, heat is mainly found on the PI-Ag surface (Fig. 6B). In the case of conventional copper substrate, due to the good thermal conductivity, heat transferred rapidly longitudinally between the layers, and thus, heat is found distributed throughout the whole substrate (Fig. 6C). In this sense, it can be revealed that the high-energy pouch cells equipped with PI-Ag-Li anode can be isolated into smaller units that block heat propagation to each other, thus restricting thermal runaway only to the small unit. Differential scanning calorimeters (DSC) measurement was conducted on Cu-20Li and PI-Ag-20Li to evaluate their thermal properties. As shown in Fig. 6D, although their exothermic peak appears at 160°C, the total heat release of PI-Ag-20Li is much lower than that of Cu-20Li (−33.5 versus −53.5 kJ g^{-1}), verifying the self-extinguishing nature of the PI-Ag anode. On the basis of these characteristics, we performed accelerating rate calorimeter (ARC) tests on 0.5-Ah pouch cells of Pi-Ag-20Li and Cu-20Li. As shown in Fig. 6E, for the pouch cell with Cu-20Li anode (green line), self-heating initiates at 121°C, thermal runaway occurs at 125°C, and the maximum temperature during thermal runaway reaches 680°C. In contrast, for the pouch cell with PI-Ag-20Li (orange line), self-heating is detected at 135°C, with no evident continuous self-heating caused by thermal runaway observed. Instead, there is a spontaneous cessation of the self-heating with nearly no heat accumulation, indicating a thermal

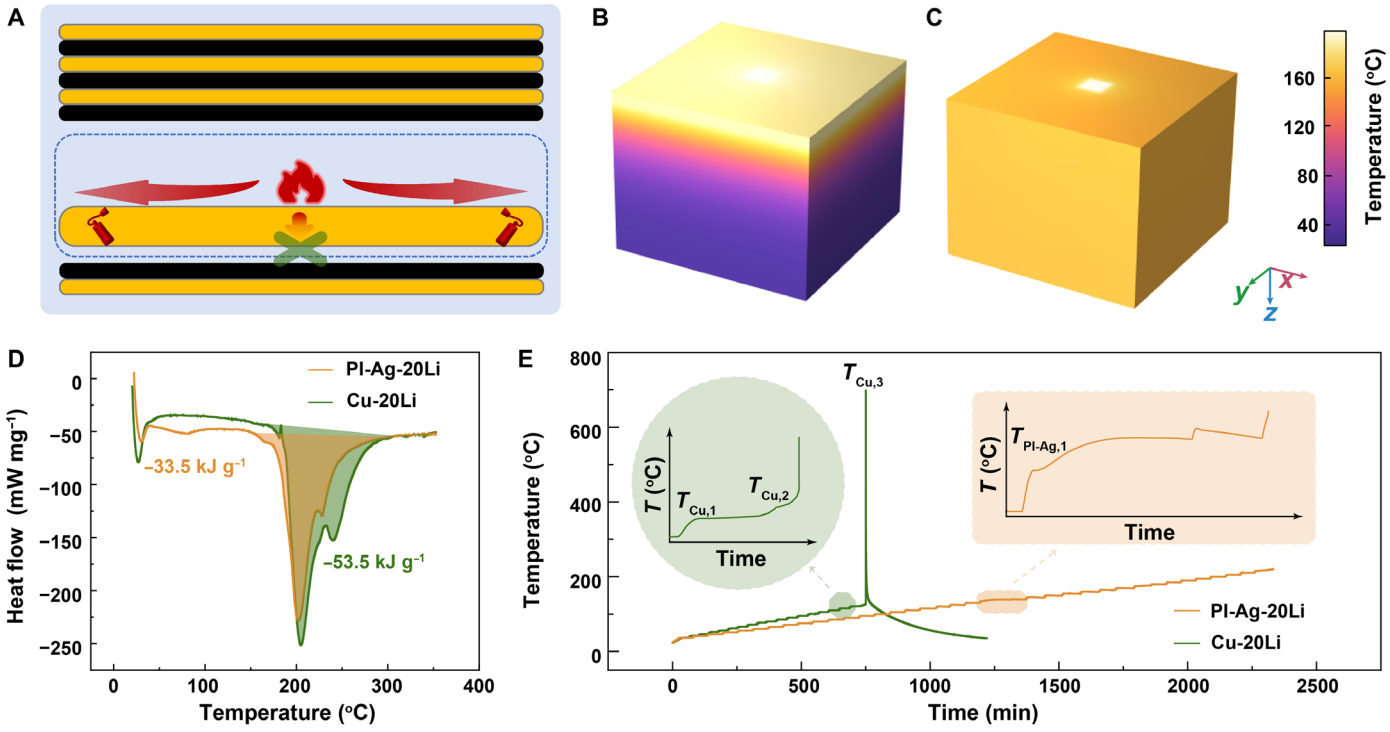

Fig. 6. Safety comparison of PI-Ag substrate anode and conventional Cu substrate anode. (**A**) Schematic representation of heat propagation blocking during thermal runaway in a multilayer electrode pouch cell using PI-Ag-Li anode. Simulations of heat transfer processes of different substrate exposed to a single heat source (T = 476 K) using COMSOL Multiphysics. (**B**) PI-Ag substrate anode and (**C**) Cu substrate anode. (**D**) DSC profiles of PI-Ag-20Li and Cu-20Li anodes in an ester electrolyte. (**E**) Voltage and temperature changes during the ARC test of a 0.5-Ah pouch cell assembled with PI-Ag-20Li or Cu-20Li anode and NCM811 cathode, where T_1 represents the onset temperature of self-heating, T_2 represents the onset temperature of thermal runaway, and T_3 represents the maximum temperature of thermal runaway.

runaway-preventing behavior. All the aforementioned results demonstrate that polyimide, owing to its thermal stability and insulating properties, can prevent the domino effect triggered by self-heating, thereby effectively suppressing thermal runaway in a battery. The high-safety feature of PI-Ag/Li integrated anode demonstrates its feasibility for use in practical high-energy batteries.

DISCUSSION

To conclude, we demonstrate an integrated, lightweight anode with improved specific energy and dual-reinforced anti-pulverization functionality for LMBs. Silver NPs monolayer was chemically immobilized on ultralight PI substrate through ion-ligand exchange reaction, and the integrated anode was realized by electrodeposition or lamination of ultrathin Li foil onto it. It is revealed that the Ag phase diffused in Li solid solution and self-evolved into a fully lithiophilic, homogeneous Li-Ag alloy, which contributes to a uniform lithium deposition and mitigated dead Li pulverization. Meanwhile, a strong chemical interaction between the bottommost Li-Ag atom and the PI matrix is built via the van der Waals bond (Li-Ag···O═C), which enables a good electrode integrity and electrical continuity upon cycling. The dual anti-pulverization property makes our integrated anode particularly attractive for a lithium-limited LMB system. As a result, full-cell pairing PI-Ag/Li anodes with NCM811 cathodes demonstrate a long-term cycling stability over 500 cycles with 80% capacity retention (N/P ratio of 5). Even under harsh conditions of high-loading cathode (20 mg cm^{-2}) and low N/P ratio (1.0), PI-Ag/Li||NCM811 full cell still maintained a remarkably stable cycling with capacity retention of 90% over 170 cycles. Compared to the most cutting-edge anode-free LMBs, the specific energy of different LMBs assembled using our PI-Ag/Li integrated anode can be increased by approximately 10%. In addition, the high-energy LMBs equipped with our integrated anode also demonstrate a superior high-safety characteristic that effectively blocked heat propagation under extreme conditions such as short circuits and thermal runaway. Our integrated anode design not only paves the way for realizing improvement in specific energy of LMBs to a higher level but also circumvents the problems of pulverization in the practical implementation of high-capacity anodes and can be extended to other alloy anodes such as Si, Al, Mg, and Zn.

MATERIALS AND METHODS

Preparation of the PI-Ag substrate

First, the PI film (8 μm, 12 cm by 12 cm) was immersed in a 5 M potassium hydroxide solution in a 20-cm diameter glass petri dish for 2 hours. The PI-K$^+$ film was then washed thoroughly with purified water and immersed in 0.02 M silver-ammonia solution for 2 hours (ammonia was dropped into 0.02 M silver nitrate solution until the precipitate disappeared). Last, the PI-Ag$^+$ film was washed and immersed into 0.2 M L-ascorbic acid solution for 2 min. The film was

washed with pure water and dried in a vacuum oven at 60°C to obtain the final PI-Ag substrate.

Preparation of PI-Ag-Li

Electrochemical lithiation was occurred in 2032-type coin cell. The working electrodes were PI-Ag and lithium foil. The electrolyte was an ether electrolyte [1.0 M LiTFSI dissolved in 1,3-Dioxolane (DOL)/Dimethoxyethane (DME) (1:1, by volume) containing 1% $LiNO_3$]. All batteries were assembled in a glove box under Ar atmosphere [$O_2 < 0.01$ parts per million (ppm), $H_2O < 0.01$ ppm]. The protocol was to discharge at the required amount of Li by Landt (CT2001A). Electrochemical lithiation of Cu-Li was also prepared by the same method. PI-Ag-20Li and Cu-20Li were obtained by rolling PI-Ag or copper foil with 20-μm Li foil in the dry room (dew point temperature < −40°C).

Electrochemical measurements

Two different areal capacities of NCM811 cathodes were prepared. Low areal capacity of NCM811 cathodes were used to probe the cycling stability of the anodes. NCM811, super P, and polyvinylidene difluoride (PVDF) were mixed in weight ratio of 8:1:1, and the active material loading was 7.5 mg cm^{-2}. NCM811 cathodes were used to probe the application of anodes in practical systems. NCM811, super P, and PVDF were mixed in weight ratio of 95:2.5:2.5, and the active material loading was 20 mg cm^{-2}. The electrolytes were ester electrolyte [1.0 M $LiPF_6$ dissolved in EC/DMC/DEC (1:1, by volume) containing 5% fluoroethylene carbonate (FEC)] and LHCE [lithium bis(fluorosulfonyl)imide (LiFSI), dimethoxyethane (DME), and 1,1,2,2-tetrafluoroethyl-2,2,3,3-tetrafluoropropylether (TTE) were mixed in a molar ratio of 1:1:3], and the amount of electrolyte added in coin cells is 6 g Ah^{-1}. All cells were assembled in a glove box under Ar atmosphere and tested by Landt (CT2001A).

Li||Cu and Li||PI-Ag half-cells

Li||Cu and Li||PI-Ag half-cells were assembled to investigate the specific role of PI-Ag in regulating lithium deposition and to evaluate the average Coulombic efficiency. The cells were fabricated by paring a lithium foil (thickness, 0.55 mm) with Cu or PI-Ag, respectively, in a 50-μl commercial ester electrolyte. The ester electrolyte contained 1 M lithium hexafluorophosphate ($LiPF_6$) in the mixture of ethylene carbonate (EC), dimethyl carbonate (DMC), and diethyl carbonate (DEC) (1:1:1 in volume and 5% FEC containing, purchased from Nanjing MJS Corp.). The Coulombic efficiency was evaluated as follows: 1 mAh cm^{-2} of Li was first deposited onto Cu or PI-Ag at 0.1 mA cm^{-2} and then stripped away by charging to 0.2 V by 2 cycles. Then, these cells were deposited 1 mAh cm^{-2} Li and galvanostatic charge/discharge under 0.1 mA cm^{-2} for 100 specific cycles and charged to 1 V again, and the average CE thus can be calculated according to the final charged capacity.

NCM811||PI-Ag-Li and NCM811||Cu-Li full cell

The full cells were composed of PI-Ag-Li or Cu-Li anode (8 mAh cm^{-2} predeposited lithium), NCM811 (7.5 mg cm^{-2}, N/P = 5), and 50 μl of commercial ester electrolyte. The ester electrolyte contained 1 M $LiPF_6$ in the mixture of EC, DMC, and DEC (1:1:1 in volume and 5% FEC containing, purchased from Nanjing MJS Corp.). The cycling test protocol is constant current constant voltage (CCCV) at 1 C rate (1 C = 200 mA g^{-1}) with the voltage window of 2.8 to 4.3 V. The rate test was conducted under constant current conditions with cycling at 0.5 C, 1 C, 2 C, 3 C, and 5 C for each, within the voltage window of 2.8 to 4.3 V.

Li||Pi-Ag-20Li and Li||Cu-20Li half-cells

The PI-Ag-20Li and Cu-20Li were fabricated by rolling a 20-μm lithium foil onto PI-Ag or Cu (referred to as PI-Ag-20Li or Cu-20Li), respectively. The Li||PI-Ag-20Li and Li||Cu-20Li half-cells were assembled by coupling PI-Ag-20Li or Cu-20Li with a 550-μm lithium foil in a 50-μl LHCE. The LHCE contains LiFSI, DME, and TTE with a molar ratio of 1:1:3. The half-cells were galvanostatic charge/discharge to evaluate the cycling stability of the anodes in the voltage range of 0 to 0.2 V (current density: 2 mA cm^{-2}, cycling capacity: 2 mAh cm^{-2}).

Lithium-less full cells: NCM811||PI-Ag-20Li, NCM811||20Li-Ag, and NCM811||Cu-20Li full cell

The full cells were assembled by coupling PI-Ag-20Li, Cu-20Li, or 20Li-Ag (20-μm Li-Ag alloy) with NCM811(20 mg cm^{-2}, N/P = 1) in a 20-μl LHCE electrolyte (6 g Ah^{-1}). The test protocol is CCCV at 0.5 C rate (1 C = 200 mA g^{-1}) over a voltage window of 2.8 to 4.3 V.

Lithium-less pouch cells: NCM811||PI-Ag-20Li

The pouch cell was fabricated in a dry room, with PI-Ag-20Li anodes (three pieces, 58 mm by 45 mm), NCM811 cathodes (two pieces, 56 mm by 43 mm), and Al_2O_3-coated separators. The LHCE electrolyte (1 g Ah^{-1}, 360 mg) was injected into the pouch cell in a glove box under the Ar atmosphere. The 0.36-Ah pouch cell was cycled over a voltage range of 2.8 to 4.3 V by Landt (CT2001A) at 0.2 C.

Characterizations

The XPS was conducted on Kratos Axis Supra with Al Ka achromatic x-ray source. Thermogravimetric analysis (STA 449F3 Jupiter) was performed with a scan rate of 10°C min^{-1}. 4,4′-Dimethoxytrityl modulus images were collected on AFM system (Bruker, Multimode 8 with Nanoscope V controllers). The SEM images were investigated by SEM (Hitachi Regulus 8100, operating at 10 kV) with an EDS system. Cross-sectional samples were prepared by focused ion beam (Helios Nanolab 600i, FEI Corp.). The electronic conductivity was obtained by four-probe tester (ST 2258C and ST2553-F01). In situ x-ray powder diffraction was performed on a Bruker D8 Adwance diffractometer with Cu Ka radiation (λ = 1.5418 Å) and Landt (CT2001A) using a specially designed Swagelok cell.

Battery safety tests

The ARC test was performed on the 0.5-Ah pouch cell with an EV-ARC system (Thermal Hazard Technology Inc.). The pouch cell was assembled in the dry room, using PI-Ag-20Li and Cu-20Li as the anodes and NCM811 as cathodes and Al_2O_3-coated separators. In addition, the LHCE electrolyte (1 g Ah^{-1}, 500 μl) was injected into the pouch cell in a glove box under Ar atmosphere. The pouch cell was charged to 4.3 V at 50 mA and followed by a constant voltage at 4.3 V held until the current decayed to 25 mA. The fully charged cell was heated in a cylindrical calorimeter during the test. The starting temperature was 50°C with a heating step of 5°C, and the temperature sensitivity was 0.02°C min^{-1} in an adiabatic environment. If the detected heating rate of the battery is less than the sensitivity setting value, then the calorimeter system will automatically enter the next "heat-wait-seek" test mode cycle; if it is greater, then the calorimeter system will automatically switch to the "adiabatic" test mode until the battery self-heating is less than the system set sensitivity value or reaches the end of the system set temperature stop. PI-Ag-Li (5 mm × 5 mm, the mass of Li was 0.163 mg) or Cu-Li (the mass of Li was

0.18 mg) was mixed with carbonate electrolyte (50 μl mg^{-1} based on the mass of Li) and sealed in a high-pressure crucible with gold plated surface. Also, the high-pressure DSC was conducted in DSC 214 Polyma of Netzsch.

DFT calculations

All DFT calculations were performed using the Vienna Ab Initio Simulation Package. The generalized gradient approximation method with the Perdew-Burke- Ernzerhof exchange-correlation function was used to manage the electron exchange and correlation energy. The plane wave basis (kinetic energy cutoff value, 450 eV) was used to describe the valence electrons. A mesh of 2 by 2 by 1 was used for the *k*-point sampling obtained from the gamma center. The thickness of the vacuum layer is 20 Å. The atomic positions were fully optimized until the energy and forces converged to 1×10^{-5} eV and 0.03 eV $Å^{-1}$, respectively. The calculations of adsorption energy were conducted as follows: $E_{ads-x} = E_1 - (E_2 + E_x)$. Where E_1 is the total energy of system with *X* adsorbed; E_2 is the energy of Li, Ag, or Li-Ag system; and E_x is the energy of Li or PI.

COMSOL Multiphysics simulations

Geometrical configuration

The composites is divided into three parts: The upper and lower layers are rectangular with a length and width of 10 μm and a height of 0.5 μm, and the middle layer is 10 μm in length and width and 7 μm in height. The monolayer material is a rectangle with a length and width of 10 μm and a height of 8 μm.

The geometry is a solid domain and the physical field is solid heat transfer. The thermal conductivity, density, and specific heat capacity data of the materials are in table S5.

Calculation method

A heat source is set up at the top of the geometry (the heat source is a square with a side length of 1 μm), and the boundary condition is the temperature, which is set to 473 K. The boundary conditions of the four faces of the geometry in terms of length-height and width-height are set to be symmetric surfaces, and it is physically assumed that the boundaries of the geometry do not affect heat transfer. The initial value of the entire computational domain is set to 298 K. The remaining faces are thermally insulating boundary conditions.

Supplementary Materials

This PDF file includes:

Figs. S1 to S26
Notes S1 to S10
Tables S1 to S5
References

REFERENCE AND NOTES

1. F. Duffner, N. Kronemeyer, J. Tübke, J. Leker, M. Winter, R. Schmuch, Post-lithium-ion battery cell production and its compatibility with lithium-ion cell production infrastructure. *Nat. Energy* **6**, 123–134 (2021).
2. J. Xiao, F. Shi, T. Glossmann, C. Burnett, Z. Liu, From laboratory innovations to materials manufacturing for lithium-based batteries. *Nat. Energy* **8**, 329–339 (2023).
3. Y. Zhang, L. Yu, X.-D. Zhang, Y.-H. Wang, C. Yang, X. Liu, W.-P. Wang, Y. Zhang, X.-T. Li, G. Li, S. Xin, Y.-G. Guo, C. Bai, A smart risk-responding polymer membrane for safer batteries. *Sci. Adv.* **9**, eade5802 (2023).
4. Y. Liu, X. Tao, Y. Wang, C. Jiang, C. Ma, O. Sheng, G. Lu, X. W. D. Lou, Self-assembled monolayers direct a LiF-rich interphase toward long-life lithium metal batteries. *Science* **375**, 739–745 (2022).
5. W. Wu, W. Luo, Y. Huang, Less is more: A perspective on thinning lithium metal towards high-energy-density rechargeable lithium batteries. *Chem. Soc. Rev.* **52**, 2553–2572 (2023).
6. R. Schmuch, R. Wagner, G. Hörpel, T. Placke, M. Winter, Performance and cost of materials for lithium-based rechargeable automotive batteries. *Nat. Energy* **3**, 267–278 (2018).
7. J. Liu, Z. Bao, Y. Cui, E. J. Dufek, J. B. Goodenough, P. Khalifah, Q. Li, B. Y. Liaw, P. Liu, A. Manthiram, Y. S. Meng, V. R. Subramanian, M. F. Toney, V. V. Viswanathan, M. S. Whittingham, J. Xiao, W. Xu, J. Yang, X.-Q. Yang, J.-G. Zhang, Pathways for practical high-energy long-cycling lithium metal batteries. *Nat. Energy* **4**, 180–186 (2019).
8. P. Albertus, S. Babinec, S. Litzelman, A. Newman, Status and challenges in enabling the lithium metal electrode for high-energy and low-cost rechargeable batteries. *Nat. Energy* **3**, 16–21 (2018).
9. A. Lal, F. You, Will reshoring manufacturing of advanced electric vehicle battery support renewable energy transition and climate targets? *Sci. Adv.* **9**, eadg6740 (2023).
10. L.-L. Lu, Y.-Y. Lu, Z.-X. Zhu, J.-X. Shao, H.-B. Yao, S. Wang, T.-W. Zhang, Y. Ni, X.-X. Wang, S.-H. Yu, Extremely fast-charging lithium ion battery enabled by dual-gradient structure design. *Sci. Adv.* **8**, eabm6624 (2022).
11. A. J. Louli, A. Eldesoky, R. Weber, M. Genovese, M. Coon, J. deGooyer, Z. Deng, R. T. White, J. Lee, T. Rodgers, R. Petibon, S. Hy, S. J. H. Cheng, J. R. Dahn, Diagnosing and correcting anode-free cell failure via electrolyte and morphological analysis. *Nat. Energy* **5**, 693–702 (2020).
12. Z. Yu, H. Wang, X. Kong, W. Huang, Y. Tsao, D. G. Mackanic, K. Wang, X. Wang, W. Huang, S. Choudhury, Y. Zheng, C. V. Amanchukwu, S. T. Hung, Y. Ma, E. G. Lomeli, J. Qin, Y. Cui, Z. Bao, Molecular design for electrolyte solvents enabling energy-dense and long-cycling lithium metal batteries. *Nat. Energy* **5**, 526–533 (2020).
13. T. Liu, J. Liu, L. Li, L. Yu, J. Diao, T. Zhou, S. Li, A. Dai, W. Zhao, S. Xu, Y. Ren, L. Wang, T. Wu, R. Qi, Y. Xiao, J. Zheng, W. Cha, R. Harder, I. Robinson, J. Wen, J. Lu, F. Pan, K. Amine, Origin of structural degradation in Li-rich layered oxide cathode. *Nature* **606**, 305–312 (2022).
14. Y. J. Guo, C. H. Zhang, S. Xin, J. L. Shi, W. P. Wang, M. Fan, Y. X. Chang, W. H. He, E. Wang, Y. G. Zou, X. A. Yang, F. Meng, Y. Y. Zhang, Z. Q. Lei, Y. X. Yin, Y. G. Guo, Competitive doping chemistry for nickel-rich layered oxide cathode materials. *Angew. Chem. Int. Ed.* **61**, e202116865 (2022).
15. Y. Ye, L.-Y. Chou, Y. Liu, H. Wang, H. K. Lee, W. Huang, J. Wan, K. Liu, G. Zhou, Y. Yang, A. Yang, X. Xiao, X. Gao, D. T. Boyle, H. Chen, W. Zhang, S. C. Kim, Y. Cui, Ultralight and fire-extinguishing current collectors for high-energy and high-safety lithium-ion batteries. *Nat. Energy* **5**, 786–793 (2020).
16. J.-L. Shi, H. Sheng, X.-H. Meng, X.-D. Zhang, D. Lei, X. Sun, H. Pan, J. Wang, X. Yu, C. Wang, Y. Li, Y.-G. Guo, Size controllable single-crystalline Ni-rich cathodes for high-energy lithium-ion batteries. *Natl. Sci. Rev.* **10**, nwac226 (2023).
17. Z. Zhang, Y. Song, B. Zhang, L. Wang, X. He, Metallized plastic foils: A promising solution for high-energy lithium-ion battery current collectors. *Adv. Energy Mater.* **13**, 2302134 (2023).
18. M. Su, G. Huang, S. Wang, Y. Wang, H. Wang, High safety separators for rechargeable lithium batteries. *Sci. China Chem.* **64**, 1131–1156 (2021).
19. R. Fang, Z. Han, J. Li, Z. Yu, J. Pan, S. Cheong, R. D. Tilley, F. Trujillo, D.-W. Wang, Rationalized design of hyperbranched trans-scale graphene arrays for enduring high-energy lithium metal batteries. *Sci. Adv.* **8**, eadc9961 (2022).
20. Y. Fang, S. L. Zhang, Z.-P. Wu, D. Luan, X. W. D. Lou, A highly stable lithium metal anode enabled by Ag nanoparticle–embedded nitrogen-doped carbon macroporous fibers. *Sci. Adv.* **7**, eabg3626 (2021).
21. R. A. House, G. J. Rees, M. A. Pérez-Osorio, J.-J. Marie, E. Boivin, A. W. Robertson, A. Nag, M. Garcia-Fernandez, K.-J. Zhou, P. G. Bruce, First-cycle voltage hysteresis in Li-rich 3D cathodes associated with molecular O_2 trapped in the bulk. *Nat. Energy* **5**, 777–785 (2020).
22. E. Hu, X. Yu, R. Lin, X. Bi, J. Lu, S. Bak, K.-W. Nam, H. L. Xin, C. Jaye, D. A. Fischer, K. Amine, X.-Q. Yang, Evolution of redox couples in Li- and Mn-rich cathode materials and mitigation of voltage fade by reducing oxygen release. *Nat. Energy* **3**, 690–698 (2018).
23. G. Assat, J.-M. Tarascon, Fundamental understanding and practical challenges of anionic redox activity in Li-ion batteries. *Nat. Energy* **3**, 373–386 (2018).
24. S. Sun, C.-Z. Zhao, H. Yuan, Z.-H. Fu, X. Chen, Y. Lu, Y.-F. Li, J.-K. Hu, J. Dong, J.-Q. Huang, M. Ouyang, Q. Zhang, Eliminating interfacial O-involving degradation in Li-rich Mn-based cathodes for all-solid-state lithium batteries. *Sci. Adv.* **8**, eadd5189 (2022).
25. Z. Wu, C. Wang, Z. Hui, H. Liu, S. Wang, S. Yu, X. Xing, J. Holoubek, Q. Miao, H. L. Xin, P. Liu, Growing single-crystalline seeds on lithiophobic substrates to enable fast-charging lithium-metal batteries. *Nat. Energy* **8**, 340–350 (2023).
26. Z. Yu, P. E. Rudnicki, Z. Zhang, Z. Huang, H. Celik, S. T. Oyakhire, Y. Chen, X. Kong, S. C. Kim, X. Xiao, H. Wang, Y. Zheng, G. A. Kamat, M. S. Kim, S. F. Bent, J. Qin, Y. Cui, Z. Bao, Rational solvent molecule tuning for high-performance lithium metal battery electrolytes. *Nat. Energy* **7**, 94–106 (2022).
27. Y. M. Zhao, F. S. Yue, S. C. Li, Y. Zhang, Z. R. Tian, Q. Xu, S. Xin, Y. G. Guo, Advances of polymer binders forsilicon-basedanodes in high energy densitylithium-ionbatteries. *InfoMat* **3**, 460–501 (2021).
28. W. Wu, J. Duan, J. Wen, Y. Chen, X. Liu, L. Huang, Z. Wang, S. Deng, Y. Huang, W. Luo, A writable lithium metal ink. *Sci. China Chem.* **63**, 1483–1489 (2020).

29. M. Mao, X. Ji, Q. Wang, Z. Lin, M. Li, T. Liu, C. Wang, Y.-S. Hu, H. Li, X. Huang, L. Chen, L. Suo, Anion-enrichment interface enables high-voltage anode-free lithium metal batteries. *Nat. Commun.* **14**, 6788 (2023).
30. C. Fang, J. Li, M. Zhang, Y. Zhang, F. Yang, J. Z. Lee, M.-H. Lee, J. Alvarado, M. A. Schroeder, Y. Yang, B. Lu, N. Williams, M. Ceja, L. Yang, M. Cai, J. Gu, K. Xu, X. Wang, Y. S. Meng, Quantifying inactive lithium in lithium metal batteries. *Nature* **572**, 511–515 (2019).
31. Y. Zhang, T.-T. Zuo, J. Popovic, K. Lim, Y.-X. Yin, J. Maier, Y.-G. Guo, Towards better Li metal anodes: Challenges and strategies. *Mater. Today* **33**, 56–74 (2020).
32. J. A. Lewis, K. A. Cavallaro, Y. Liu, M. T. McDowell, The promise of alloy anodes for solid-state batteries. *Joule* **6**, 1418–1430 (2022).
33. Y. Wen, J. Ding, J. Liu, M. Zhu, R. Hu, A separator rich in $_{SnF2and}$ NO3—directs an ultra-stable interface toward high performance Li metal batteries. *Energ. Environ. Sci.* **16**, 2957–2967 (2023).
34. J. C. Guo, S. J. Tan, C. H. Zhang, W. P. Wang, Y. Zhao, F. Wang, X. S. Zhang, R. Wen, Y. Zhang, M. Fan, S. Xin, J. Zhang, Y. G. Guo, A self-reconfigured, dual-layered artificial interphase toward high-current-density quasi-solid-state lithium metal batteries. *Adv. Mater.* **35**, e2300350 (2023).
35. P. Shi, Z.-H. Fu, M.-Y. Zhou, X. Chen, N. Yao, L.-P. Hou, C.-Z. Zhao, B.-Q. Li, J.-Q. Huang, X.-Q. Zhang, Q. Zhang, Inhibiting intercrystalline reactions of anode with electrolytes for long-cycling lithium batteries. *Sci. Adv.* **8**, eabq3445 (2022).
36. Y. Lu, C.-Z. Zhao, R. Zhang, H. Yuan, L.-P. Hou, Z.-H. Fu, X. Chen, J.-Q. Huang, Q. Zhang, The carrier transition from Li atoms to Li vacancies in solid-state lithium alloy anodes. *Sci. Adv.* **7**, eabi5520 (2021).
37. D. Li, F. Chu, Z. He, Y. Cheng, F. Wu, Single-material aluminum foil as anodes enabling high-performance lithium-ion batteries: The roles of prelithiation and working mechanism. *Mater. Today* **58**, 80–90 (2022).
38. C. Niu, D. Liu, J. A. Lochala, C. S. Anderson, X. Cao, M. E. Gross, W. Xu, J.-G. Zhang, M. S. Whittingham, J. Xiao, J. Liu, Balancing interfacial reactions to achieve long cycle life in high-energy lithium metal batteries. *Nat. Energy* **6**, 723–732 (2021).
39. S. Jin, Y. Ye, Y. Niu, Y. Xu, H. Jin, J. Wang, Z. Sun, A. Cao, X. Wu, Y. Luo, H. Ji, L.-J. Wan, Solid–solution-based metal alloy phase for highly Reversible Lithium metal anode. *J. Am. Chem. Soc.* **142**, 8818–8826 (2020).
40. B. D. Adams, J. Zheng, X. Ren, W. Xu, J. G. Zhang, Accurate determination of coulombic efficiency for lithium metal anodes and lithium metal batteries. *Adv. Energy Mater.* **8**, 1702097 (2017).
41. C. Luo, H. Hu, T. Zhang, S. Wen, R. Wang, Y. An, S. S. Chi, J. Wang, C. Wang, J. Chang, Z. Zheng, Y. Deng, Roll-to-roll fabrication of zero-volume-expansion lithium-composite anodes to realize high-energy-density flexible and stable lithium-metal batteries. *Adv. Mater.* **34**, e2205677 (2022).
42. Z. Huang, J.-C. Lai, S.-L. Liao, Z. Yu, Y. Chen, W. Yu, H. Gong, X. Gao, Y. Yang, J. Qin, Y. Cui, Z. Bao, A salt-philic, solvent-phobic interfacial coating design for lithium metal electrodes. *Nat. Energy* **8**, 577–585 (2023).
43. M. Shang, O. G. Shovon, F. E. Y. Wong, J. Niu, A BF_3^-doped MXene dual-layer interphase for a reliable lithium-metal anode. *Adv. Mater.* **35**, 2210111 (2022).
44. S. Li, J. Huang, Y. Cui, S. Liu, Z. Chen, W. Huang, C. Li, R. Liu, R. Fu, D. Wu, A robust all-organic protective layer towards ultrahigh-rate and large-capacity Li metal anodes. *Nat. Nanotechnol.* **17**, 613–621 (2022).
45. H. Zhang, S. Ju, G. Xia, X. Yu, Identifying the positive role of lithium hydride in stabilizing Li metal anodes. *Sci. Adv.* **8**, eabl8245 (2022).
46. S. Huang, Z. Wu, B. Johannessen, K. Long, P. Qing, P. He, X. Ji, W. Wei, Y. Chen, L. Chen, Interfacial friction enabling $\lesssim 20\ \mu$m thin free-standing lithium strips for lithium metal batteries. *Nat. Commun.* **14**, 5678 (2023).
47. M. Zhang, K. Liu, Y. Gan, H. Wang, F. Liu, M. Bai, X. Tang, Z. Wang, S. Li, A. Shao, K. Zhou, T. Wang, Z. Wang, S. Yuan, Y. Ma, Boosting the temperature adaptability of lithium metal batteries via a moisture/acid-purified, ion-diffusion accelerated separator. *Adv. Energy Mater.* **12**, 2201390 (2022).
48. L. P. Buchwalter, B. D. Silverman, L. Witt, A. R. Rossi, X-ray photoelectron spectroscopy analysis of hexafluorodianhydride–oxydianiline polyimide: Substantiation for substituent effects on aromatic carbon 1sbinding energies. *J. Vac. Sci. Technol. A* **5**, 226–230 (1987).
49. W. M. Haynes. CRC Handbook of Chemistry and Physics. 92nd Edition (CRC Press, 2007), vol. 12, p. 216–217.

Acknowledgments

Funding: This work was supported by the Basic Science Center Project of National Natural Science Foundation of China (grant no. 52388201), the National Key R&D Program of China (grant no. 2021YFB2500301), the CAS Project for Young Scientists in Basic Research (grant no. YSBR-058), the National Science Foundation of China (grant nos. 22379149 and 22309187), the Beijing Natural Science Foundation (grant nos. JQ22005 and Z220021), the Young Elite Scientists Sponsorship Program by CWAST (grant no. 2022QNRC001), the China Postdoctoral Science Foundation (grant no. 2021 M703268), and Junior Fellow Program of Beijing National Laboratory for Molecular Sciences (grant no. 2021BMS20062). **Author contributions:** Conceptualization: C.-H.Z., J.Z., L.-J.W., and Y.-G.G. Data curation: C.-H.Z. Formal analysis: C.-H.Z., S.-J.T., and Y.-J.G. Funding acquisition: S.-J.T., J.Z., S.X., and Y.-G.G. Investigation: C.-H.Z., Y.-J.G., J.-C.G., and X.-S.Z. Methodology: C.-H.Z. and Y.-G.G. Project administration: J.Z., L.-J.W., and Y.-G.G. Resources: B.-Z.L., L.-J.W., and Y.-G.G. Supervision: J.Z., L.-J.W., and Y.-G.G. Validation: C.-H.Z., Y.-H.W., and Y.-F.T. Visualization: C.-H.Z. Writing—original draft: C.-H.Z. Writing—review and editing: C.-H.Z., J.Z., S.X., Y.-J.G., L.-J.W., Y.-G.G. **Competing interests:** The authors declare that they have no competing interests. **Data and materials availability:** All data needed to evaluate the conclusions in the paper are present in the paper and/or the Supplementary Materials.

Submitted 20 October 2023
Accepted 23 February 2024
Published 29 March 2024
10.1126/sciadv.adl4842